

Landslides (2020) 17:1283–1296
 DOI 10.1007/s10346-020-01364-z
 Received: 23 January 2019
 Accepted: 28 January 2020
 Published online: 10 February 2020
 © Springer-Verlag GmbH Germany
 part of Springer Nature 2020

Adam M. Booth · Justin C. McCarley · Joann Nelson

Multi-year, three-dimensional landslide surface deformation from repeat lidar and response to precipitation: Mill Gulch earthflow, California

Abstract Slow-moving landslides are often the dominant process that shapes hillslopes and delivers sediment to channels in weak lithologies. Understanding what controls their velocities is therefore essential for deciphering their role in landscape evolution and estimating hazards. In this study, we used four sequential airborne lidar data sets to derive the three-dimensional (3D), 1-m spatial resolution surface velocity field of the Mill Gulch earthflow, northern California, for three periods of time spanning a decade. Phase correlation, an image processing technique, applied to the precisely aligned lidar digital elevation models confidently resolved horizontal velocities from 0.2 to 5 m year⁻¹. The velocity field defined three distinct kinematic zones of the landslide with different sensitivities to precipitation, such that the head moved slowly at 0.3–0.5 m year⁻¹, the transport zone moved fastest at 2–5 m year⁻¹, and a forked toe moved intermittently at 0–4 m year⁻¹. Inverting the 3D surface velocity field to infer landslide thickness suggested that the head was underlain by a 6-m-deep, concave-up slip surface, while the transport zone likely had a 1–2.5-m-deep translational slip surface. We hypothesized that velocity in the head was least sensitive to changing precipitation because of its greater inferred depth, which likely dampened the amplitude of pore pressure fluctuations. A lack of major head scarp retrogressions also may have contributed to the relatively steady velocity in the head, while buttressing and debuttressing interactions between the landslide's toes and the creek running in Mill Gulch may have contributed to the more dramatic changes in velocity in the transport zone and toes. Although predicting landslide velocity from precipitation data alone may therefore be challenging, producing detailed 3D deformation fields from repeat topographic data can be an important tool for deciphering interactions between internal controls, such as changes to landslide geometry, and external controls, such as climate, on landslide motion.

Keywords Mill gulch earthflow · Image correlation · Repeat lidar · 3D change detection · Landslide mechanics

Introduction

In mountainous regions with weak lithologies, slow-moving landslides are often the dominant process that erodes hillslopes and delivers sediment to channels (Kelsey 1978, 1980; Mackey and Roering 2011; Scheingross et al. 2013; Simoni et al. 2013; Bennett et al. 2016). Although many of such landslides move slowly or intermittently for years to millennia (Swanson and Swanston 1977; Bovis and Jones 1992; Mackey et al. 2009), they may suddenly accelerate and fail catastrophically, which can be hazardous to lives and infrastructure (Miller and Sias 1998; Wartman et al. 2016; Handwerger et al. 2019). Monitoring landslide movements to improve our understanding of the processes that control motion is therefore essential to determine how landslide erosion rates

respond to climatic and tectonic forcing over geologic time and estimate hazards on human time scales. In this study, we used image correlation on four sequential aerial lidar data sets spanning a decade to document the high-resolution, three-dimensional (3D) surface deformation field of a slow-moving landslide along the northern California coast. We then analyzed those displacement fields and the inferred landslide thickness alongside precipitation data to interpret plausible relationships between climate and the landslide's motion.

Over geologic time scales, landslides can exert a strong influence on the evolution of landscapes by directly shaping hillslopes and affecting sediment supply to channels. At the range scale, landslides are the main hillslope erosion mechanism that can keep pace with high uplift rates in mountainous, non-glaciated regions, and in doing so they set the maximum hillslope relief and topographic gradient of a landscape (Schmidt and Montgomery 1995; Burbank et al. 1996; Larsen and Montgomery 2012). At a finer scale, landslides coevolve with low-order channels, thereby suppressing development of a regular drainage network and lengthening hillslopes (Tarolli and Dalla Fontana 2009; Booth and Roering 2011; Booth et al. 2013b). Where landslides infringe on higher-order channels, they often create dams that affect the pattern of channel erosion and deposition for many kilometers along the river, and these effects can persist for thousands of years or more (Ouimet et al. 2007; Safran et al. 2011).

Over shorter time scales, landslide movement rates and patterns are a first-order control on hazard and sediment delivery to channels. In many cases, threshold values of precipitation or pore pressure required to trigger landslide movement have been identified (e.g., Prior and Stephens 1972; Iverson and Major 1987; Handwerger et al. 2013), and furthermore, landslide movement rates have been shown to correlate with pore pressure in some cases (e.g., Coe et al. 2003; Corominas et al., 2005). However, not all landslides show a clear relationship between precipitation or pore pressure and movement thresholds or rates (van Asch 2005; Massey et al. 2013, 2016). The observation that landslides may or may not respond predictably to precipitation highlights the importance of quantitatively documenting spatial and temporal patterns of landslide displacements in order to infer their controlling mechanisms.

Multi-temporal remote sensing techniques are becoming widely applied for landslide monitoring, especially for large, slow-moving landslides (Delacourt et al. 2007; Tofani et al. 2013). Ground-based techniques that require direct access to a landslide, such as differential GPS or GNSS (e.g., Malet et al. 2002; Coe et al. 2003), strain gauges, or borehole inclinometers (e.g., Mikkelsen 1996) can have high accuracy, precision, and temporal resolution, but typically have low spatial resolution due to access and cost constraints. The main advantage of remote sensing data is higher spatial resolution,

and three types of air- or space-based multi-temporal remote sensing products have especially contributed to advancing landslide monitoring studies: optical images, synthetic aperture radar (SAR), and airborne lidar (Tofani et al. 2013).

Optical imagery can have centimeter-scale resolution, and repeat imagery has been successfully used to monitor landslide movements with manual feature tracking (e.g., Mackey and Roering 2011) and image correlation techniques (e.g., Delacourt et al. 2004; Lacroix et al. 2015; Roering et al. 2015). Image correlation has also been widely applied to measure glacier deformation (e.g., Bindschadler and Scambos 1991; Kääb 2002) and fault slip (e.g., Van Puymbroeck et al. 2000). Although displacements measured with optical images are usually 2D, traditional photogrammetry and structure-from-motion (SfM) techniques can produce digital elevation models to quantify geomorphic changes (e.g., Del Soldato et al. 2018; Riquelme et al. 2019) or surface displacements in 3D (Casson et al. 2005; Lucieer et al. 2013).

Satellite-based differential interferometric SAR (D-InSAR) can measure landslide displacements with centimeter-scale precision in the satellite line-of-sight direction over weekly to monthly time scales, which has proven useful for time series analysis of landslide deformation (e.g., Handwerger et al. 2015; Tong and Schmidt 2016; Intieri et al. 2018). Recently, airborne D-InSAR has been able to measure 3D displacement fields of landslides by optimizing flight paths to resolve three independent components of surface displacements (Delbridge et al. 2016; Handwerger et al. 2019). The persistent scatterer (PS) technique, which tracks features with distinctive amplitudes in the SAR images, has also successfully been used to map slow-moving landslide displacements and produce time series (e.g., Hilley et al. 2004; Bianchini et al. 2018; Cohen-Waeber et al. 2018; Solari et al. 2018). Combining ascending and descending orbits with PS can also resolve 3D surface displacements in some cases (Raucoules et al., 2013).

The main strengths of airborne lidar for landslide monitoring are its high spatial resolution, which is typically 1 m or better, and especially its ability to penetrate gaps in the vegetation to image the ground surface itself in 3D (Corsini et al. 2007; Jaboyedoff et al. 2010; Daehne and Corsini 2012). Due to relatively high costs, acquisition of repeat lidar data is rare compared with optical images and SAR, with typically on the order of years between data sets. Airborne lidar is routinely used for change detection analysis, in which digital elevation models (DEMs) are differenced vertically to measure volume changes (Burns et al. 2010; Ventura et al. 2011; DeLong et al. 2012). More recently, repeat airborne lidar has been used to measure the 3D displacement fields of slow-moving landslides, which is not possible with other remote sensing techniques in vegetated areas (Daehne and Corsini 2012; Booth et al. 2018). In this study, we specifically advance the use of repeat airborne lidar data to measure landslide surface deformation in 3D and at high spatial resolution to determine how multi-year precipitation relates to landslide motion.

Study site and methods

Study site: Mill Gulch earthflow, California

The Mill Gulch earthflow is a 450-m-long and 50–100-m-wide slow-moving landslide located 2 km southeast of Fort Ross on the northern California coast (Fig. 1a, b). The landslide is best described as a “composite earth slide-earth flow” (Cruden and

Varnes 1996), as movement likely occurs through a combination of frictional slip on a discrete basal failure surface and flow, where internal deformation is distributed throughout the landslide’s body (Manson et al. 2006). Such landslides are widespread throughout the northern California Coast Ranges (Keefer and Johnson 1983; Mackey and Roering 2011; Bennett et al. 2016) and commonly referred to as “earthflows.” The upper part of the Mill Gulch landslide has a typical earthflow geometry consisting of an amphitheater-shaped head below an arcuate head scarp, which transitions to a narrower, gullied transport zone downslope (Kelsey 1978). The transport zone of the Mill Gulch earthflow then diverges into two smaller, bulbous toes that end in Mill Gulch at the foot of the slope.

The landscape in the vicinity of the landslide reflects the regional tectonic and geologic setting. The right-lateral San Andreas Fault (SAF) runs northwest-southeast between the landslide and the coast (Fig. 1a), subparallel to the coastline and to the regional trend of the main range crests. This segment of the fault ruptured during the 1906 San Francisco earthquake and was offset by approximately 3 m (Lawson 1908). The SAF juxtaposes interbedded sandstones and mudstones of Miocene age to the southwest against late Eocene to late Cretaceous wacke of the Franciscan Complex to the northeast (Blake et al. 2002). Deep-seated landslides are widespread in the Franciscan Complex rocks, especially where those units intersect the coast and near the SAF (Manson et al. 2006). Mill Gulch extends 3 km from a prominent ridge to the Pacific Ocean to the southwest and is offset by 80–100 m across the SAF (Muhs et al. 2003). Southwest of the fault, the stream has incised approximately 35 m through an uplifted marine terrace. The lowest marine terrace at Fort Ross has been correlated to the lowest terrace at Point Arena, to the north of the study area, which has been dated to the 80-ka Marine Isotope Stage 5a sea-level high stand (Muhs et al. 1994, 2003; Arrowsmith and Crosby 2006). This yields an uplift rate of 0.4 mm year⁻¹, which is typical for coastal northern California (Muhs et al. 1992; Bowles and Cowgill 2012; DeLong et al. 2017). Cosmogenic radionuclide-derived, catchment-averaged erosion rates in nearby Russian Gulch and the Gualala River watershed are lower at 0.2 mm year⁻¹, and the Mill Gulch earthflow itself was responsible for 0.3 mm year⁻¹ of erosion from 2003 to 2007, averaged over the entire area of the Mill Gulch catchment (DeLong et al. 2012, 2017).

Coastal northern California has a Mediterranean climate with dry summers and most precipitation falling as rain from October to May. Monthly precipitation data at Fort Ross was available from the California Department of Water Resources for the 2003 through 2013 water years of the study period, but 19 months of data were missing from that 132-month record. To fill in those gaps, we correlated the monthly precipitation at Fort Ross with monthly precipitation at Venado, 23 km northeast of the landslide, which was the closest station with continuously available data (Fig. 2). A linear fit was given by

$$\text{FRR} = 0.75 + 0.58\text{VEN} \quad (1)$$

where FRR is precipitation at Fort Ross and VEN is precipitation at Venado, measured in centimeters, which explained 89% of the variance with the largest discrepancies occurring for the wettest months when precipitation exceeded 30 cm at Venado. We used

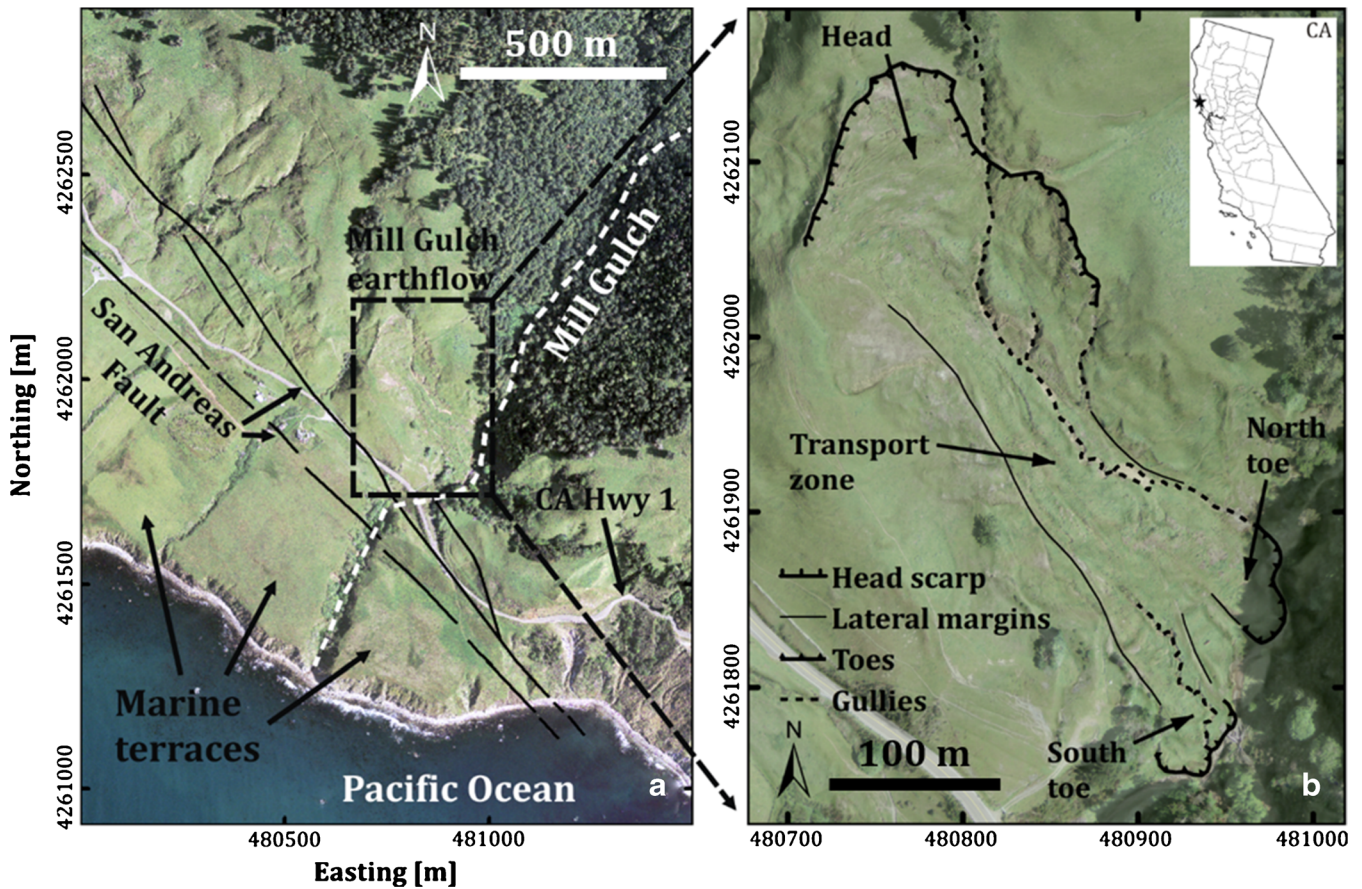


Fig. 1 a Orthorectified aerial photograph taken April 9, 2011, of the area surrounding the Mill Gulch earthflow. b The earthflow annotated with its main morphologic features interpreted from the aerial photo and lidar data (“Lidar processing and alignment”)

that linear fit to estimate monthly precipitation at Fort Ross when no data were available there and produce a continuous precipitation time series to compare to the landslide’s surface velocity.

Lidar processing and alignment

To measure the earthflow’s 3D surface displacements, we used four airborne lidar data sets collected in February 2003, April 2007, September 2010, and October 2013 (Table 1). These data sets are publicly available through the National Science Foundation-supported OpenTopography Facility (<https://opentopography.org/>) and the National Oceanic and Atmospheric Administration’s Digital Coast program (<https://coast.noaa.gov/digitalcoast/>). Although each of these data sets was independently georeferenced by the vendor responsible for the lidar acquisition, to measure the relative displacements between each collection date as precisely as possible, we realigned and gridded the raw point clouds as follows. First, we extracted all points classified as ground returns in a 350×500 -m box centered on the landslide. The average ground point densities for each cloud ranged from 0.9 to 4.9 pts. m^{-2} (Table 1). We then used the iterative closest point algorithm (Besl and McKay 1992), implemented in the open-source software CloudCompare (<http://www.cloudcompare.org/>), to precisely align each point cloud with that of the previous date, using all points on the stable terrain surrounding the active landslide. The number of points used for each alignment was 635,724 (2003–2007 alignment) or

798,585 (2007–2010 and 2010–2013 alignments). The average root-mean-square error (RMSE) on these alignments was 0.4 m (Table 1), which we take as an estimate of the overall relative uncertainty on the position of each point that includes instrumental error, point spacing, and error due to different points on the irregular ground surface being imaged in each lidar scan (Oppikofer et al. 2009).

We then interpolated each aligned point cloud to a 1-m resolution DEM using the natural neighbor algorithm (Sibson 1981), which is well suited to gridding lidar data for three reasons (Sambridge et al. 1995). First, the elevation interpolated at a point depends only on its nearest neighbors, which limits spatial correlation of errors and works well on irregularly spaced points with varying spatial density. Second, the interpolated surface is continuously differentiable, which ensures that topography varies smoothly from point to point on the interpolated grid. Third, the interpolated elevation exactly matches the elevation of the original data points at those coordinates. We chose 1 m spatial resolution because it corresponded to the lowest ground point densities of the 2003 and 2010 data sets.

3D surface deformation fields

A landslide’s 3D surface deformation field is defined by the x -, y -, and z -components of its surface displacements, which can be described in two different reference frames that differ in their

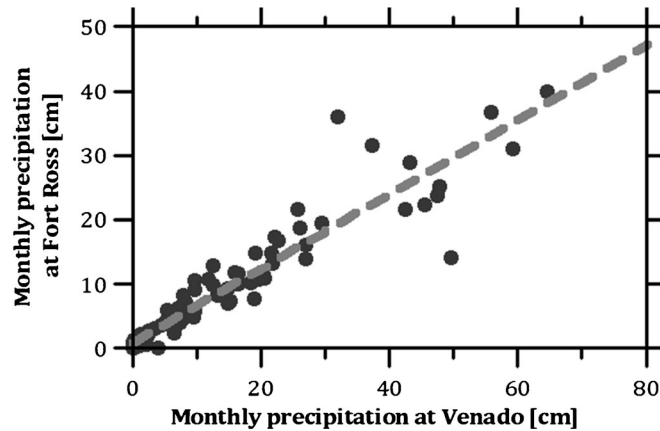


Fig. 2 Monthly precipitation measured at Fort Ross (FRR) vs. monthly precipitation at Venado (VEN) from 1999 to 2018. Dashed line is a linear fit used to estimate precipitation at Fort Ross during months when no data were available there

representation of the vertical component of motion (Delbridge et al. 2016). In an Eulerian reference frame, the vertical component of displacement is defined at each fixed point in space and can be measured directly by vertically differencing two DEMs. Horizontal displacements can then be measured independently to complete the 3D surface displacement field (Casson et al. 2005; Daehne and Corsini 2012; Booth et al. 2013a, 2018). In a Lagrangian reference frame, the vertical component of displacement is instead defined as the elevation change each point experienced as it moved from one location on the landslide to another. The 3D surface displacement field can therefore be measured directly by tracking the displacement of a feature in a 3D point cloud (Teza et al. 2007; Oppikofer et al. 2009), or the vertical component can be measured by interpolating the elevations at each end of a horizontal displacement vector and then differencing them (Aryal et al. 2015; Avouac and Leprince 2015). In this study, we determined 3D surface displacements in both reference frames, with the Eulerian reference frame results presented in the main article and Lagrangian reference frame results presented in the [Supplementary Material](#). We highlight results in the Eulerian reference frame because vertical changes to the land surface elevation can be measured everywhere, independent of whether or not horizontal displacements are defined.

To measure the horizontal components of the earthflow's displacement field, we used the phase correlation method, a common image correlation technique, on the aligned DEMs. Phase

correlation depends on the Fourier shift theorem, which states that the relative offset of two images can be determined from the phase difference of their Fourier transforms (Leprince et al. 2007; Oppenheim and Schaffer 2010). Specifically, it calculates the correlation coefficient, C , as a function of possible offsets in the x - and y -directions, i and j , respectively, as

$$C(i, j) = \mathcal{F}^{-1} \left(\frac{\mathcal{Z}_1(\omega_x, \omega_y) \mathcal{Z}_2^*(\omega_x, \omega_y)}{|\mathcal{Z}_1(\omega_x, \omega_y) \mathcal{Z}_2^*(\omega_x, \omega_y)|} \right) \quad (2)$$

where $\mathcal{Z}_{1, 2}$ denotes the Fourier transform of the first or second image, ω_x, ω_y denotes frequency in the x - or y -direction, the asterisk indicates the complex conjugate, and the vertical bars indicate the magnitude (Kuglin and Hines 1975; Brown 1992; Heid and Käab 2012). The location of the peak in the correlation coefficient matrix then defines the relative offset between the two images, which has subpixel precision by interpolating C . We implemented Eq. (2) in a moving window routine following the open-source program ImGRAFT (Messerli and Grinsted 2015) to measure the offset of the window centered at each location in each pair of sequential DEMs. Specifically, for each pixel in the first DEM, we defined a $24 \text{ m} \times 24 \text{ m}$ window centered on that pixel and computed C for all offsets within a $48 \text{ m} \times 48 \text{ m}$ search window centered on that same

Table 1 Summary of lidar data properties

Year	Data set name	Average point spacing (pts m^{-2})	Number of points used for alignment	RMSE on alignment to previous date (m)
2003	Northern San Andreas Fault ^a	0.9	–	–
2007	EarthScope Northern California LiDAR project ^a	1.9	635,724	0.39
2010	California Coastal Conservancy Lidar ^b	1.0	798,585	0.36
2013	UMD-NASA Carbon Mapping/Sonoma County Vegetation Mapping and LiDAR Program ^a	4.9	798,585	0.43

^a Available from OpenTopography

^b Available from NOAA Digital Coast

pixel in the second DEM. While choice of these window sizes is arbitrary (Delacourt et al. 2007; Avouac and Leprince 2015), at the Mill Gulch study site smaller windows tended to produce high numbers of physically incorrect displacement measurements due to lidar data uncertainty, while larger window sizes tended to overly smooth the abrupt changes in displacement at the boundaries of the earthflow (Supplementary Material). Physically incorrect displacements were identified as being greater than several meters in length in randomly distributed orientations, including uphill, on the landslide as well as on stable parts of the study area.

The phase correlation technique assumes rigid body translation with no rotation, which may be violated by many parts of a landslide's heterogeneous displacement field, and we made several modifications to the technique to produce reliable displacement fields for the Mill Gulch earthflow. First, we applied a low-pass filter to the Fourier spectra that excluded all frequencies greater than the Nyquist frequency, which was 0.5 m^{-1} for our 1-m-resolution DEMs (Booth et al. 2018). We then excluded locations that had a poorly defined peak in the correlation coefficient matrix, C , which otherwise led to physically incorrect displacements such as in the upslope direction or with a drastically different magnitude than neighboring locations. Those poorly defined correlation coefficient matrices had several isolated peaks of similar magnitude corresponding to different offsets, while well-defined peaks consisted of a cluster of high correlation coefficients centered on the true offset (Booth et al. 2018). Applying the criterion that the highest and second highest coefficients in C had to be adjacent to one another to be considered a well-defined peak effectively filtered out the majority of the physically incorrect displacements in a single step. Alternatively, applying a threshold signal strength or signal-to-noise ratio of the correlation coefficients to identify incorrect displacements (Delacourt et al. 2004) did not eliminate most of the physically incorrect displacements at our study site. Furthermore, we avoided making direct assumptions about landslide behavior by using the general properties of the correlation coefficient matrix itself to exclude incorrect displacements, rather than retroactively using characteristics of the displacement field (Lacroix et al. 2015).

To complete the 3D surface displacement fields, vertical elevation changes in an Eulerian reference frame were measured by subtracting each pair of DEMs. Vertical components of landslide displacements in a Lagrangian reference frame were measured by subtracting the final elevation from the starting elevation of each horizontal displacement vector (Supplementary Material).

Earthflow slip surface inversion

Landslide surface displacements measured in 3D may be used qualitatively (Hutchinson 1983; Casson et al. 2005; Guerriero et al. 2017) and quantitatively to infer the basal slip surface geometry (Booth et al. 2013a; Aryal et al. 2015; Delbridge et al. 2016). Quantitative approaches are based on conservation of mass, which states that at every point on the landslide (in an Eulerian reference frame),

$$\frac{\partial(\rho h)}{\partial t} = -\nabla \cdot (\rho \mathbf{q}) + \dot{\varepsilon} \quad (3)$$

where ρ is the depth-averaged density of the landslide material, h is landslide thickness, t is time, \mathbf{q} is horizontal flux per unit width, and $\dot{\varepsilon}$ is the rate of direct addition or removal of mass due to deposition or erosion, respectively. Expanding the derivatives in Eq. (3) results in

$$h \frac{\partial \rho}{\partial t} + \rho \frac{\partial h}{\partial t} = -\rho \frac{\partial q_x}{\partial x} - \rho \frac{\partial q_y}{\partial y} - q_x \frac{\partial \rho}{\partial x} - q_y \frac{\partial \rho}{\partial y} + \dot{\varepsilon} \quad (4)$$

where q_x and q_y indicate the x - and y -components of \mathbf{q} , which highlights the relative importance of changes in flux, changes in density, and direct surface deposition or erosion on the landslide thickness. On the left hand side of Eq. (4), the first term describes a change in mass due to a change in density of landslide material with time, and the second term describes a change in mass due to a change in thickness with time. Those changes in mass are balanced by the terms on the right-hand side of Eq. (4), which are the contributions of spatial gradients in the flux (first two terms), spatial gradients in the density (third and fourth terms), and direct deposition or erosion (last term). Although density may in general vary spatially or with time as landslide material dilates or compacts, those gradients are likely much smaller than gradients in the flux at the Mill Gulch earthflow. For example, the bulk modulus of clay-rich landslide debris is typically of order 10^7 Pa (U.S. Army Corps of Engineers 1990), indicating that a given change in pressure causes a roughly seven order of magnitude smaller change in the relative density. Assuming changes to pressure at the slip surface of a 1–10-m-deep landslide are the same magnitude as the lithostatic pressure at those depths (Delbridge et al. 2016), relative changes in density should be less than 1%. Similarly, dilation of a clay-rich shear zone is expected to cause at most just a few centimeters of vertical thickening (Iverson 2005), which would cause a change in depth-averaged density of about 1% for a landslide that is of order meters deep. Overall, the contribution of those changes in density to changes in the landslide thickness is small compared with measured elevation changes of up to 0.5 m year^{-1} in magnitude at the Mill Gulch earthflow (“3D displacement fields”) and likely much less than the vertical uncertainty of the airborne lidar data. Direct deposition or erosion is also likely negligible on nearly all the landslide surfaces over the decadal time scale of this study, except in localized gullies where overland flow of water is possible during intense rainstorms and at the faces of the toes where they are directly exposed to stream erosion by the creek running in Mill Gulch. Those locations occupy less than 1% of the landslide's surface area and therefore have a minimal effect of the overall inversion procedure described below, which weights all locations on the landslide equally. To further minimize the effects of direct surface erosion or deposition on the thickness inversion, we only inverted the well-defined velocity field from 2007 to 2010, which was when the landslide moved the least and when precipitation was lowest, suggesting limited overland flow in gullies.

Following Booth et al. (2013a), we therefore drop the terms in Eq. (4) that involve density gradients and direct erosion or deposition, which implies conservation of volume rather than mass:

$$\frac{\partial h}{\partial t} = -\nabla \cdot (\bar{\mathbf{u}}h), \quad (5)$$

where \bar{u} is the depth-averaged landslide velocity. Equation (5) extends the established balanced cross-section approach that has been previously applied to landslides to estimate their depths at the head scarp or toe (Hutchinson 1983; Bishop 1999) to the entire landslide. Since repeat lidar is capable of measuring changes to the landslide's surface, we further assumed that the change in landslide thickness was equivalent to the change in its surface elevation, z , at a point, and that the depth-averaged velocity was equal to the measured horizontal surface velocity, u_{surf} leading to

$$\frac{\partial z}{\partial t} = -\nabla \cdot (u_{\text{surf}} h). \quad (6)$$

Setting $\bar{u} = u_{\text{surf}}$ assumes that at every point on the landslide deformation occurs by sliding on a narrow shear zone with material above transported as a rigid plug, as is commonly observed for earthflows (Keefer and Johnson 1983). Relaxing this assumption to allow for a thicker shear zone and implying a more flow-like behavior would proportionately increase the inferred landslide thickness at all points, but would not change the spatial pattern of thickness variations (Booth et al. 2013a, b). We measured $\partial z/\partial t$ by differencing the DEMs in the vertical direction and measured u_{surf} with the phase correlation technique ("3D surface deformation fields"). We then rearranged Eq. (6) as a system of linear equations and solved for h that minimizes the value of

$$\|Ah - b\|^2 + \alpha^2 \|\nabla^2 h\|^2 \quad (7)$$

where A is a diagonally dominant matrix containing the velocity data, b is a vector containing the change in elevation data, and α is a damping parameter (Booth et al. 2013a), which we chose by the L-curve method (Aster et al., 2011; Delbridge et al., 2016). In summary, the resulting inferred thickness represents the best model that does not violate conservation of volume, assumes the surface velocity equals the depth-averaged velocity, and is consistent with the uncertainty of the measured elevation changes. Since inversion of Eq. (6) does not incorporate possible changes in density, direct surface erosion or deposition, multiple active slip surfaces at different depths, or deformation by flow, we refer to the resulting thickness as the "inferred thickness" to be consistent with the assumptions described above.

Results

3D displacement fields

Horizontal surface displacement rates of the Mill Gulch earthflow greater than 0.2 m year^{-1} and less than 5 m year^{-1} were confidently measured with the phase correlation technique (Fig. 3a–c). We defined the horizontal minimum detectable displacement (MDD) and MDD rate for each time interval as three times the standard deviation (99% confidence) of apparent displacements or rates, respectively, measured on the stable hillslopes and marine terraces to the south and west of the active earthflow (Table 2). While image correlation can in theory be much more precise, the MDD in this case was limited by the uncertainty of the airborne lidar data. The maximum measured displacement of 20 m, corresponding to a rate of 5 m year^{-1} , was limited by changes to the ground surface texture due to landslide deformation. Only small patches

of the landslide surface that traveled downslope as relatively coherent blocks and contained distinctive surface features were measured at that maximum displacement. Vertical displacement rates greater than an MDD rate of 0.06 m year^{-1} (Table 2) in an Eulerian reference frame were measured over most of the landslide's surface and ranged up to 0.5 m year^{-1} in magnitude (Fig. 3d–f). The vertical MDD was also defined as three times the standard deviation of apparent vertical changes of the stable areas. The large apparent vertical changes along the eastern boundary of the study site, as well as some spurious horizontal displacements and areas of no data, are largely artifacts due to interpolation of low ground return density lidar data under thick forest cover (Fig. 1). Vertical displacement rates measured in a Lagrangian reference frame ranged up to 2 m year^{-1} in magnitude, and generally followed the local topographic gradient (Supplementary Material, Fig. S2).

The spatial pattern of horizontal displacements in all three time intervals corresponded to the main morphologic features of the earthflow. The head moved slowly to the south as a relatively coherent mass at a rate of less than 1 m year^{-1} . The transition from the head to the narrower transport zone was abrupt at an arcuate internal scarp (Fig. 3b), and rates downslope of that scarp were much faster at up to 5 m year^{-1} to the southeast. Horizontal displacements were undefined over large areas of the transport zone in 2003–2007 and 2010–2013 when displacements were greatest, especially near its boundaries, where non-rigid deformation of the landslide material changed the surface texture substantially (Fig. 4), resulting in poorly defined correlation coefficient peaks. However, large measurable vertical changes at those locations indicated that those parts of the landslide were also active. At the landslide's toe, horizontal movement rates were slower than those of the transport zone and ranged from less than the MDD rate to 4 m year^{-1} .

The spatial pattern of vertical deformation was consistent with the spatial pattern of horizontal displacements, indicating deflation of the head and transport zone of the landslide and accumulation in the two toes. At long length scales, vertical displacements were generally negative, indicating downward motion, in the head and transport zone, and generally positive in the toes of the earthflow. At shorter length scales of several meters, localized vertical changes resulted from individual landslide hummocks and other surface roughness elements translating downslope (Fig. 4c). Direct erosion or deposition in localized areas, such as at the downslope faces of the landslide's toes and in the creek flowing through Mill Gulch, also occurred (e.g., Fig. 3e), but was not detectable on the surface of the landslide itself.

Over the 10-year time period of the study, the earthflow's head moved at a relatively constant rate ($0.3\text{--}0.5 \text{ m year}^{-1}$), but movement of the transport zone and toe varied dramatically with time ($0\text{--}5 \text{ m year}^{-1}$). We selected five small patches of terrain (Fig. 3c) where horizontal displacements were defined for each time interval to construct a time series of landslide movement rates representative of the head, transport zone, and south toe (Fig. 5; Table 3). For comparison, Fig. 5 also shows a time series of cumulative monthly precipitation for each water year at Fort Ross ("Study site: Mill Gulch earthflow, California").

From 2003 to 2007, the patch centered in the landslide's head moved to the south at $0.5 \pm 0.1 \text{ m year}^{-1}$ (mean \pm standard deviation), while the three transport zone patches moved to the

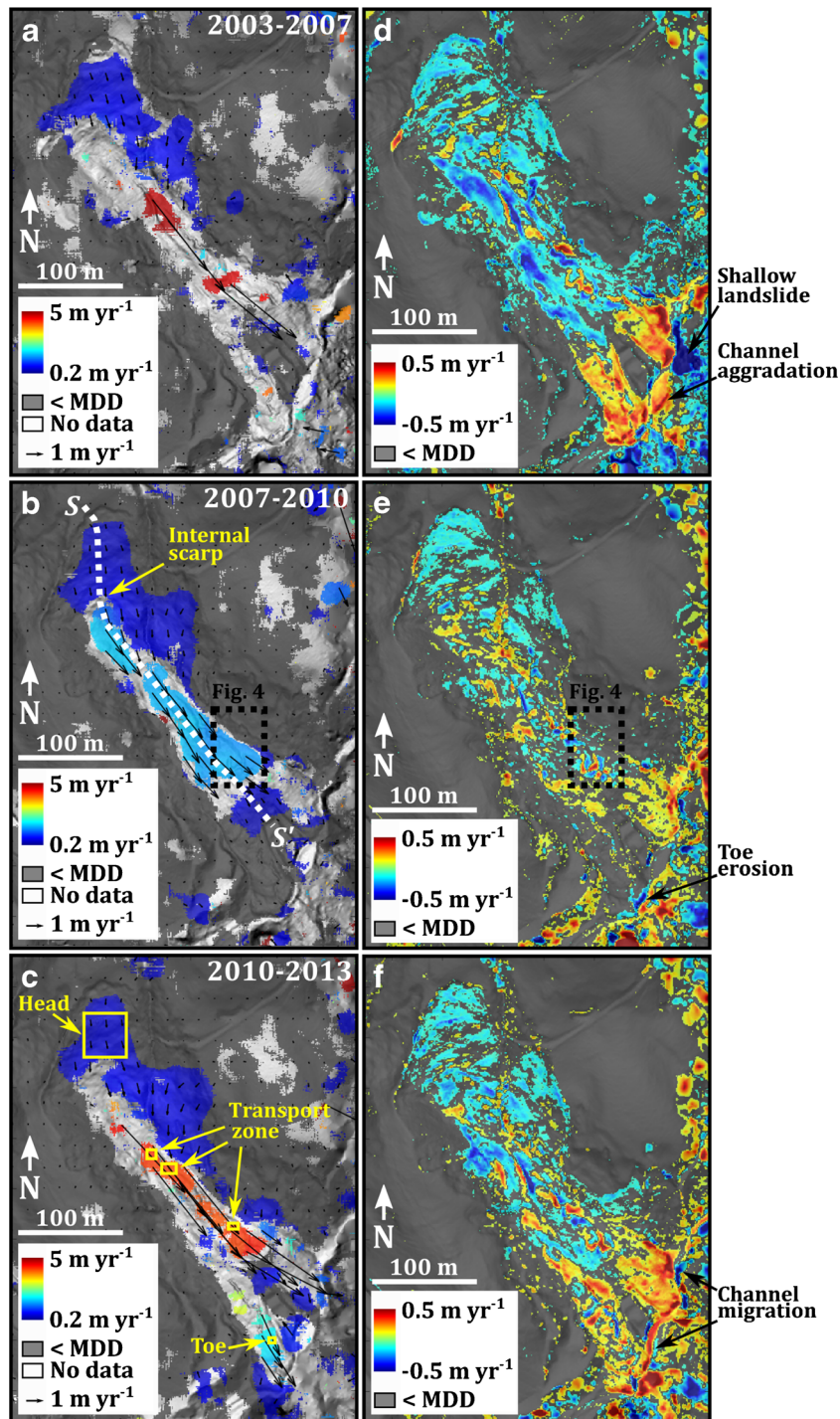


Fig. 3 Lidar-derived slope maps overlain with a subsample of velocity vectors and colored according to the magnitude of the horizontal velocity (a–c) or rate of vertical elevation change (d–f) of the Mill Gulch earthflow for three time intervals between 2003 and 2013. Dashed black boxes in b and e indicate extend of Fig. 4. Yellow boxes labeled Head, Transport zone, and Toe in c are patches used to generate the velocity time series in Fig. 5. Profile SS' in b is a streamline used to show the inferred landslide thickness in Fig. 6

southeast at $4.7 \pm 0.1 \text{ m year}^{-1}$ (Fig. 5; Table 3). Over large areas of the transport zone, horizontal displacements were undefined during this time interval, but the broad pattern of relatively large vertical changes there indicated that substantial movement took place (Fig. 3a, d). Specifically, the surface elevation decreased at

rates as high as 0.5 m year^{-1} throughout the head and transport zone, and the two toes increased in surface elevation and advanced into Mill Gulch. The small patch with defined displacements on the south toe moved more slowly than the transport zone at $3.9 \pm 0.01 \text{ m year}^{-1}$, and surface uplift over the entire toe indicated that

Table 2 Minimum detectable displacements (MDD) and rates

Time interval	MDD (m)		MDD rate (m year ⁻¹)	
	Horizontal	Vertical	Horizontal	Vertical
2003–2007	0.79	0.27	0.19	0.06
2007–2010	0.59	0.20	0.17	0.06
2010–2013	0.54	0.18	0.18	0.06

movement also occurred outside of that patch. The north toe also experienced surface uplift at a rate of up to 0.5 m year^{-1} . A shallow landslide occurred on the east bank of Mill Gulch directly across from the north toe, likely contributing sediment that aggraded the channel upstream of the south toe (Fig. 3d; DeLong et al. 2012). Seasonal precipitation was slightly below to well above average during this time period with Fort Ross receiving 83%, 86%, 95%, and 152% of average each water year (Fig. 5; Table 3).

From 2007 to 2010, the entire landslide slowed down, with the head moving at $0.3 \pm 0.1 \text{ m year}^{-1}$, the transport zone moving at $1.5 \pm 0.03 \text{ m year}^{-1}$, and the south toe at $0.1 \pm 0.01 \text{ m year}^{-1}$, which is less than the MDD rate, suggesting that it had stopped (Fig. 5; Table 3). Horizontal displacements were defined over most of the landslide's surface during this time interval, highlighting the abrupt change in velocity from the landslide's head to transport zone, where the movement direction changed from south to southeast, and the rate increased by a factor of 5 over a distance of just a few meters. The head of the earthflow continued to decrease in surface elevation over this time interval, while the transport zone's overall surface elevation remained steady, with downslope translation of meter-scale

roughness elements causing localized positive or negative changes (Fig. 4c). While the south toe was not moving during this time interval, its downslope face was eroded by the creek running in Mill Gulch (Fig. 3e). However, the north toe remained active, advancing into Mill Gulch and increasing its surface elevation. Due to changes to the surface texture, horizontal displacement rates of the north toe were again undefined. Precipitation was considerably below average to average over this interval of time with Fort Ross receiving 71%, 78%, 64%, and 103% of average each water year (Fig. 5; Table 3).

From 2010 to 2013, the entire landslide was active again, moving faster than in 2007–2010, but slower than in 2003–2007. The head moved at a rate of $0.4 \pm 0.05 \text{ m year}^{-1}$, the transport zone at a rate of $4.1 \pm 0.1 \text{ m year}^{-1}$, and the south toe at a rate of $1.8 \pm 0.01 \text{ m year}^{-1}$. Like in 2003–2007, both the head and transport zone broadly decreased in surface elevation, and both toes increased in surface elevation as they advanced into Mill Gulch. Localized areas of bank erosion and aggradation indicate that the active channel in Mill Gulch migrated laterally where it interacted with the landslide's toes during this time period (Fig. 3f). Precipitation was below average during this period with Fort

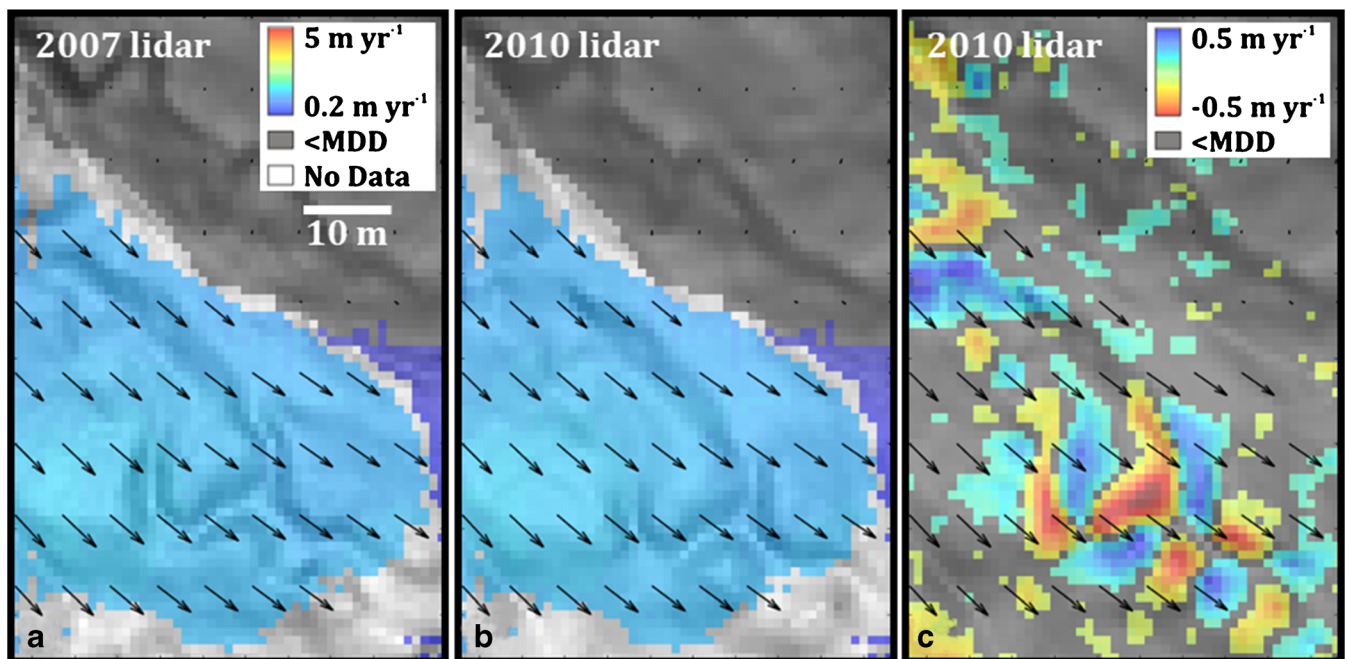


Fig. 4 Detail maps of black dashed box in Fig. 3b and e showing horizontal (a, b) and vertical (c) displacement rates of part of the Mill Gulch earthflow's transport zone for 2007–2010. Displacement vectors are shown as their actual length at the scale of the image. Backgrounds are lidar derived slope maps from 2007 (a) or 2010 (b, c). An abandoned gully feature can be clearly seen translating to the southeast on the landslide's surface (a, b), and the shape of this feature causes a pattern of alternating negative and positive elevation changes (c)

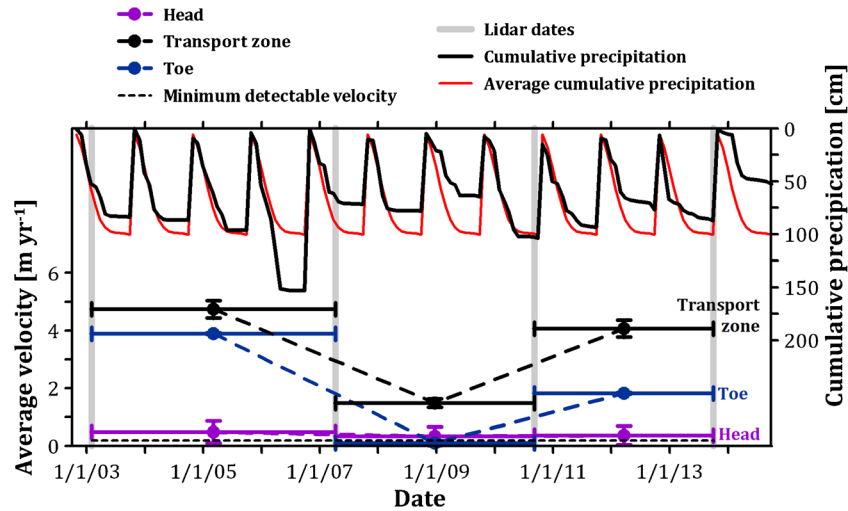


Fig. 5 Time series of average velocity (left axis) of the head, transport zone, and toe of the Mill Gulch earthflow, and cumulative monthly precipitation (right axis) by water year at Fort Ross. Horizontal error bars indicate the time intervals between lidar acquisitions over which velocities were averaged, and vertical error bars indicate the standard deviation of velocity

Ross receiving 92%, 76%, and 87% of average each water year (Fig. 6; Table 3).

Earthflow slip surface geometry and sediment flux

We performed the landslide slip surface inversion using the 2007–2010 displacement field, which had the best-defined horizontal velocity field of the three time intervals studied. This well-defined velocity field suggests that changes in the depth-averaged density of landslide material and direct surface erosion or deposition that could change the surface texture were small, such that our conservation of volume approach (“Earthflow slip surface inversion”) is reasonable for inferring the landslide’s thickness at that time. We prepared the velocity field for the inversion by manually masking the few remaining small patches of terrain with physically incorrect displacements that the filtering process (“3D surface deformation fields”) did not identify. We then used natural neighbor interpolation to fill in the undefined horizontal velocities and produce a complete 1-m resolution displacement field for the inversion.

Profile SS’ (Fig. 3b) is a streamline that follows the velocity field down the center of the earthflow, and it illustrates the main characteristics of the inferred slip surface geometry and earthflow sediment flux per unit width, defined as the landslide thickness multiplied by the surface horizontal velocity (Fig. 6 (Eulerian reference frame) and Fig. S3 (Lagrangian reference frame)). Starting at the head scarp of the earthflow, located at 15 m along profile SS’, the depth to its inferred slip surface increased in the

downslope direction until reaching a maximum of 6 m at 50 m along profile SS’ near the center of the landslide’s head. Although we do not have independent estimates of the landslide’s thickness because of access constraints, the dip of the inferred failure plane matched the dip of the exposed head scarp, providing an important independent check that the inversion results were reasonable (Fig. 6b; Fig. S3b). Head scarp erosion that would reduce its slope was not detected from the four lidar data sets and was likely minimal over the decadal time scale of this study (Avouac 1993; Hanks 2000), but the scarp’s dip should conservatively be considered a close lower bound on its initial dip. Sediment flux also increased in the downslope direction from 15 to 75 m along profile SS’, reaching a local maximum of 2 m² year⁻¹ at the lower part of the earthflow’s head (Fig. 6a). Farther downslope, the earthflow’s inferred thickness decreased to 1 m at the internal scarp (Fig. 3b), located at 110 m along profile SS’, indicating that the head had a rotational component to its motion. Sediment flux reached a local minimum of 1 m² year⁻¹ at the internal scarp. Depth to the inferred slip surface then increased gradually in the downslope direction to 2.5 m in the lower part of the transport zone, from 110 to 330 m along profile SS’, before shallowing to zero at the downslope end of the transport zone near the inactive south toe. The transport zone of the landslide was therefore predominantly a translational failure. Sediment flux also increased gradually with distance through the transport zone to reach a maximum of 3.5 m² year⁻¹ on the lower part of the transport zone before decreasing to zero at the inactive toe.

Table 3 Summary of landslide velocities and precipitation

Time interval	Head velocity (m year ⁻¹)	Transport zone velocity (m year ⁻¹)	Toe velocity (m year ⁻¹)	Percent of average precipitation in water year
2003–2007	0.5 ± 0.1	4.7 ± 0.1	3.9 ± 0.01	83%, 86%, 95%, 152%
2007–2010	0.3 ± 0.1	1.5 ± 0.03	< MDD rate	71%, 78%, 64%, 103%
2010–2013	0.4 ± 0.05	4.1 ± 0.1	1.8 ± 0.01	92%, 76%, 87%

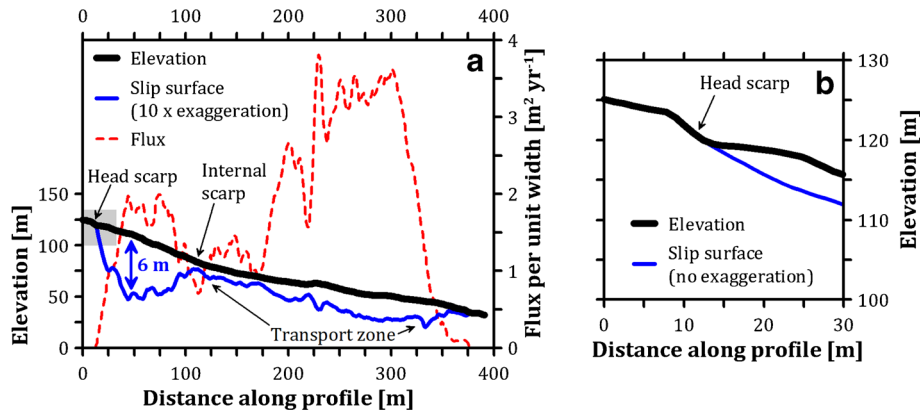


Fig. 6 a Profiles of land surface elevation and slip surface position (left axis) and sediment flux (right axis) along profile SS' (Fig. 3b) estimated by inverting the 2007–2012 3D surface displacement field. b Zoom-in of gray shaded box in a of land surface elevation and slip surface position shown with no vertical exaggeration at the head scarp

Discussion

Evaluation of image correlation for measuring landslide displacements

Our results demonstrate that image correlation of repeat airborne lidar DEMs is capable of producing 3D, high-resolution (of order 1 m), and high-precision (± 0.5 m horizontal and ± 0.2 m vertical) landslide displacement fields. As repeat airborne lidar data become increasingly available, and this technique becomes more widely applicable, several considerations are important to take into account to ensure useful results at other sites. First, the uncertainty of the lidar data limits the MDD, rather than the image correlation technique itself, which can be accurate to a small fraction of a pixel dimension (Leprince et al. 2007). For correlation of airborne lidar data in general, we therefore expect an MDD of a few decimeters. Second, the maximum measureable displacements are instead likely to be highly variable depending on how site-specific landslide kinematics and superimposed sediment transport processes affect the ground surface texture. This variability was apparent within our study site, where the technique was capable of measuring at least 20 m of total displacement where the landslide moved coherently with little disruption to the surface texture, but did not successfully measure comparable or smaller displacements elsewhere. The main areas where displacements were undefined were areas where the surface texture changed dramatically, resulting in poor correlation coefficients. This issue was most prevalent in areas with large displacements, areas of non-rigid landslide deformation, such as shear, shortening, extension, or rotation indicated by spatial gradients in the velocity field (Figs. 3a–c and 4a, b), and localized areas of direct surface erosion, such as the faces of the landslide's toes. Although the earthflow's surface was not forested, other parts of study area that had low lidar ground point densities also produced undefined or unreliable displacements. Last, selecting ground returns, aligning, and interpolating lidar point clouds likely influences the ability of image correlation techniques to measure displacements, especially if different procedures are used to process each data set. Filtering for ground returns and interpolating can affect the surface texture, while misaligned data sets can introduce systematic biases in the measured offsets. Nonetheless, quickly correlating independently gridded and georeferenced lidar DEMs over broad areas as they

become available may be sufficient as a reconnaissance tool for active landslide identification.

Comparison with previous work

Our 3D surface displacement fields were consistent with previous work on the Mill Gulch earthflow that used the same 2003 and 2007 lidar data sets to document vertical changes with DEM differencing and estimate horizontal displacements with manual feature tracking (DeLong et al. 2012). For example, DeLong et al. (2012) estimated an average velocity of 0.5 m year^{-1} in the earthflow's head, and a maximum velocity of 5 m year^{-1} in the transport zone, compared with our phase correlation-derived average velocity measurements of $0.5 \pm 0.1 \text{ m year}^{-1}$ and $4.7 \pm 0.1 \text{ m year}^{-1}$, respectively. That study also estimated a net loss of sediment from the earthflow and the hillslope opposite its toe of 3800 m^3 by integrating the elevation changes over the area of the earthflow. That calculation included contributions from both the shallow landslide on the southeast side of Mill Gulch (Fig. 3d) and the Mill Gulch earthflow itself, which experienced toe erosion and possibly overland flow erosion in gullies. Using our average inferred landslide thickness of 2.5 m, average velocity of 4.7 m year^{-1} , and width of 60 m in the transport zone, we roughly estimate that 3000 m^3 of sediment translated through the transport zone over that same time period. This suggests that the Mill Gulch earthflow and the shallow landslide on the southeast side of Mill Gulch lost more sediment than was moved through the earthflow's transport zone. That discrepancy likely resulted from a combination of the inclusion of sediment mobilized by the shallow landslide on the southeast side of Mill Gulch and possible localized gully erosion, which is thought to be typical of northern California earthflows (Kelsey 1978; Mackey and Roering 2011). However, by extending our analysis through two additional time periods to span a total of 10 years, we have shown that the Mill Gulch earthflow's 3D velocity field is highly heterogeneous in both space and time, such that its behavior over a time span of several years may not be representative of its longer-term contribution to the catchment's sediment budget. In the following section, we suggest plausible mechanisms that may contribute to the observed changes in the velocity field.

Controls on landslide motion

Forecasting a landslide's response to changing climate is an important goal of hazard analysis and for predicting sediment delivery to channels (Crozier 2010). While previous work has shown that a landslide's threshold for initiating movement or its movement rate can be predicted from climatic data (Iverson and Major 1987; Coe 2012; Zerathe et al. 2016), other studies have documented more complex responses (Allison and Brunsten 1990; van Asch 2005; Massey et al. 2013; Schulz et al. 2018). The Mill Gulch earthflow generally moved faster during wetter periods of time (Fig. 5), but different parts of the landslide were more or less sensitive to changes in multi-year precipitation, and movement rates did not clearly correspond entirely to that precipitation. Specifically, total seasonal precipitation was below to above normal at 83%, 86%, 95%, and 152% of average each water year during the first time period of the study when the landslide moved the fastest; precipitation was below normal to approximately normal at 71%, 78%, 64%, and 103% of average during the second time period when the landslide moved the slowest; and then precipitation was less than normal at 92%, 76%, and 87% of average during the last time period when the landslide moved at an intermediate rate (Table 3). The head of the landslide was least sensitive to precipitation changes, as its velocity varied by $\pm 25\%$ despite seasonal precipitation varying from 64 to 152% of average. In contrast, the transport zone velocity dropped from 4.7 to 1.5 m year^{-1} during the second time period of drier conditions, but then accelerated to 4.1 m year^{-1} , nearly its previous high rate, during a period of below average seasonal precipitation. The south toe stopped moving completely during the driest second time period, but then reactivated to move at about half its previous velocity during the following average to dry years.

We interpret that the different zones of the landslide were more or less sensitive to precipitation because of three main mechanisms. First, the landslide's inferred thickness varied from the 6-m-deep head to the 1–2.5-m-deep transport zone, which likely affected the magnitude and timing of pore pressure response to infiltrating precipitation (Reid 1994). Since the magnitude of pore pressure response decays exponentially with depth, in the deep head pore pressure may be relatively insensitive to precipitation changes, allowing that part of the slide to move steadily down slope with driving and resisting stresses approximately balanced. Pore pressures at the shallower inferred slip surface of the transport zone likely fluctuated more strongly with precipitation, causing the effective normal stress, and therefore frictional strength, to similarly fluctuate. Since the south toe was not detectably active from 2007 to 2010, its thickness was not inferred, but we hypothesize that its active thickness is similar to that of the transport zone since its velocity was also more sensitive to multi-year precipitation patterns than the head. Pore pressure response decreasing with depth is consistent with pore pressure measurements at comparable depths in another nearby earthflow in the Franciscan Complex rocks of northern California (Iverson and Major 1987) and similar clay-rich, landslide-prone slopes (Berti and Simoni 2010, 2012). Second, changes to the stress field as mass is redistributed within an earthflow and its geometry changes can obscure climatically driven changes to the effective normal stress, especially for small earthflows that experience toe erosion or head scarp retrogression (Bovis and Jones 1992; Booth et al. 2018). For example, sediment accumulation in Mill Gulch from 2003 to 2007

may have buttressed the south toe and contributed to it stopping during 2007–2010, while subsequent toe erosion may have debuttressed it and contributed to its reactivation during 2010–2013 (Fig. 3d, e). In contrast, there were no major retrogressions of the head scarp during the study period, and the head moved at a relatively constant rate. Third, antecedent moisture conditions may also affect the landslide's response to precipitation and obscure a possible relationship between multi-year velocity and average precipitation. For example, periods of drought have been shown to produce preferential flow paths for water to infiltrate earthflows and cause them to respond more rapidly to precipitation compared with more typical climatic conditions (Mcsaveney and Griffiths 1987). Such a mechanism may explain the observation that the transport zone moved nearly as fast during a dry to average climatic period that followed several years of dry conditions (4.1 m year^{-1} from 2010 to 2013) as it moved during a wet time period (4.7 m year^{-1} from 2003 to 2007). Specifically, the velocity was only 15% faster during 2003–2007, which included a year with 152% of average precipitation, than during 2010–2013. Expanding the velocity time series with other remote sensing data sets and additional lidar data to span a wider range of climatic conditions may help determine whether or not the earthflow's velocity can be predicted from precipitation data.

Conclusions

We measured the 3D and 1-m spatial resolution surface velocity field of the Mill Gulch earthflow in coastal northern California using publicly available repeat airborne lidar collected in 2003, 2007, 2010, and 2013. To measure horizontal displacements, we used phase correlation, an image processing technique, on the precisely aligned DEMs. To measure vertical displacements in an Eulerian reference frame we subtracted the DEMs, and to measure vertical displacements in a Lagrangian reference frame we differenced starting and ending elevations of the horizontal displacement vectors. The minimum detectable velocity was 0.2 m year^{-1} (horizontal) or 0.06 m year^{-1} (vertical), and horizontal velocities of up to 5 m year^{-1} were confidently measured where landslide deformation was well approximated by rigid body translation. The earthflow's head moved steadily at 0.3–0.5 m year^{-1} on an inferred 6-m-deep, concave-up slip surface, then thinned to 1–2.5 m deep and was faster at 1.5–4.7 m year^{-1} through its transport zone, which supplied sediment flux to two intermittently active toes terminating in Mill Gulch. Comparing the landslide's velocity to monthly precipitation data showed that it moved fastest during 2003–2007 when seasonal precipitation was 83%, 86%, 95%, and 152% of average in each water year, slowest during 2007–2010 when precipitation was 71%, 78%, 64%, and 103% of average, and at an intermediate rate during 2010–2013 when precipitation was 92%, 76%, and 87% of average. Although velocity broadly corresponded to precipitation, different parts of the landslide were more or less sensitive to changing precipitation. We hypothesized that the landslide's head was least sensitive to changing precipitation because of its inferred greater depth and lack of major head scarp retrogressions that could perturb the stress field. Conversely, the transport zone and south toe were likely more sensitive to changing precipitation because of their inferred shallower depth, and their velocities may have also been more variable due to buttressing and debuttressing interactions with the creek running in Mill Gulch. These results suggest that predicting the landslide's

response to future climate may be challenging, but analyzing repeat, high-resolution, 3D surface velocity fields may be a useful technique for constraining the roles of internal forcing, such as changes to landslide geometry, and external forcing, such as climate, in affecting landslide motion.

Acknowledgments

We thank the editors and four anonymous reviewers for offering constructive criticism that improved the manuscript. Lidar data are available from OpenTopography or NOAA Digital Coast, while precipitation data are available from the California Department of Water Resources.

References

- Allison RJ, Brunsden D (1990) Some mudslide movement patterns. *Earth Surf Process Landf* 15:297–311. <https://doi.org/10.1002/esp.3290150402>
- Arrowsmith JR, Crosby C (2006) Application of lidar data to constraining a late Pleistocene slip rate and vertical deformation of the northern San Andreas Fault, Fort Ross to Mendocino, California: Collaborative research between Arizona State University and the U.S. Geological Survey. USGS National Earthquake Hazards Reduction Program, Final Technical Report 06HQGR0032
- Aryal A, Brooks BA, Reid ME (2015) Landslide subsurface slip geometry inferred from 3-D surface displacement fields. *Geophys Res Lett* 42:1411–1417. <https://doi.org/10.1002/2014gl062688>
- van Asch TWJ (2005) Modelling the hysteresis in the velocity pattern of slow-moving earth flows: the role of excess pore pressure. *Earth Surf Process Landf* 30:403–411. <https://doi.org/10.1002/esp.1147>
- Aster RC, Borchers B, Thurber CH (2011) *Parameter estimation and inverse problems*, vol 90. Elsevier Academic Press, Boston, Mass
- Avouac JP (1993) Analysis of scarp profiles: evaluation of errors in morphologic dating. *J Geophys Res Solid Earth* 98(B4):6745–6754. <https://doi.org/10.1029/92JB01962>
- Avouac JP, Leprince S (2015) Geodetic imaging using optical systems. In: Schubert G (ed) *Treatise on geophysics*, 2nd edn. Elsevier, Oxford, pp 387–424
- Bennett GL, Miller SR, Roering JJ, Schmidt DA (2016) Landslides, threshold slopes, and the survival of relict terrain in the wake of the Mendocino triple junction. *Geology* 44:363–366. <https://doi.org/10.1130/G37530.1>
- Berti M, Simoni A (2010) Field evidence of pore pressure diffusion in clayey soils prone to landsliding. *J Geophys Res Earth Surf* 115(F3). <https://doi.org/10.1029/2009JF001463>
- Berti M, Simoni A (2012) Observation and analysis of near-surface pore-pressure measurements in clay-shales slopes. *Hydrol Process* 26(14):2187–2205. <https://doi.org/10.1002/hyp.7981>
- Besl PJ, McKay ND (1992) A method for registration of 3-D shapes. *IEEE Trans Pattern Anal Mach Intell* 14:239–256. <https://doi.org/10.1109/34.121791>
- Bianchini S, Raspini F, Solari L, Del Soldato M, Ciampalini A, Rosi A, Casagli N (2018) From picture to movie: twenty years of ground deformation recording over Tuscany region (Italy) with satellite InSAR. *Front Earth Sci* 6:177. <https://doi.org/10.3389/feart.2018.00177>
- Bindschadler RA, Scambos TA (1991) Satellite-image-derived velocity field of an Antarctic ice stream. *Science* 252(5003):242–246. <https://doi.org/10.1126/science.252.5003.242>
- Bishop KM (1999) Determination of tranlational landslide slip surface depth using balanced cross sections. *Environ Eng Geosci* V(2):147–156
- Blake Jr MC, Graymer RW, Stamski RE (2002) Geologic map and map database of western Sonoma, northernmost Marin, and southernmost Mendocino counties, California. *Miscellaneous Field Studies Map MF-2402*, United States Geological Survey. <https://doi.org/10.3133/mf2402>
- Booth AM, Roering JJ (2011) A 1-D mechanistic model for the evolution of earthflow-prone hillslopes. *J Geophys Res* 116. <https://doi.org/10.1029/2011Jf002024>
- Booth AM, Lamb MP, Avouac J-P, Delacourt C (2013a) Landslide velocity, thickness, and rheology from remote sensing: La Clapière landslide, France. *Geophys Res Lett* 40:4299–4304. <https://doi.org/10.1002/grl.50828>
- Booth AM, Roering JJ, Rempel AW (2013b) Topographic signatures and a general transport law for deep-seated landslides in a landscape evolution model. *J Geophys Res Earth Surf* 118:603–624. <https://doi.org/10.1002/jgrf.20051>
- Booth AM, McCarley J, Hinkle J, Shaw S, Ampuero J-P, Lamb MP (2018) Transient reactivation of a deep-seated landslide by undrained loading captured with repeat airborne and terrestrial lidar. *Geophys Res Lett* 45:4841–4850. <https://doi.org/10.1029/2018gl077812>
- Bovis MJ, Jones P (1992) Holocene history of earthflow mass movements in south-central British Columbia: the influence of hydroclimatic changes. *Can J Earth Sci* 29:1746–1755. <https://doi.org/10.1139/E92-137>
- Bowles CJ, Cowgill E (2012) Discovering marine terraces using airborne lidar along the Mendocino-Sonoma coast, northern California. *Geosphere* 8:386–402. <https://doi.org/10.1130/ges00702.1>
- Brown LG (1992) A survey of image registration techniques. *Comput Surv* 24:325–376
- Burbank DW, Leland J, Fielding E, Anderson RS, Brozovic N, Reid MR, Duncan C (1996) Bedrock incision, rock uplift and threshold hillslopes in the northwestern Himalayas. *Nature* 379:505–510. <https://doi.org/10.1038/379505a0>
- Burns WJ, Coe JA, Kaya BS, Ma L (2010) Analysis of elevation changes detected from multi-temporal LiDAR surveys in forested landslide terrain in western Oregon. *Environ Eng Geosci* 16(4):315–341. <https://doi.org/10.2113/gsegeosci.16.4.315>
- Casson B, Delacourt C, Allemand P (2005) Contribution of multi-temporal remote sensing images to characterize landslide slip surface – application to the “La Clapière” landslide (France). *Nat Hazard Earth Syst Sci* 5:425–437
- Coe JA (2012) Regional moisture balance control of landslide motion: implications for landslide forecasting in a changing climate. *Geology* 40:323–326. <https://doi.org/10.1130/G32897.1>
- Coe JA, Ellis WL, Godt JW, Savage WZ, Savage JE, Michael JA, Kibler JD, Powers PS, Lidke DJ, Debray S (2003) Seasonal movement of the Slumgullion landslide determined from Global Positioning System surveys and field instrumentation, July 1998–March 2002. *Eng Geol* 68:67–101. [https://doi.org/10.1016/S0013-7952\(02\)00199-0](https://doi.org/10.1016/S0013-7952(02)00199-0)
- Cohen-Waeber J, Bürgmann R, Chaussard E, Giannico C, Ferretti A (2018) Spatiotemporal patterns of precipitation-modulated landslide deformation from independent component analysis of InSAR time series. *Geophys Res Lett* 45(4):1878–1887. <https://doi.org/10.1002/2017GL075950>
- Corominas J, Moya J, Ledesma A, Lloret A, Gili JA (2005) Prediction of ground displacements and velocities from groundwater level changes at the Vallcebre landslide (Eastern Pyrenees, Spain). *Landslides* 2(2):83–96. <https://doi.org/10.1007/s10346-005-0049-1>
- Corsini A, Borgatti L, Coren F, Vellico M (2007) Use of multitemporal airborne lidar surveys to analyse post-failure behaviour of earth slides. *Can J Remote Sens* 33(2):116–120. <https://doi.org/10.5589/m07-015>
- Crozier MJ (2010) Deciphering the effect of climate change on landslide activity: a review. *Geomorphology* 124:260–267. <https://doi.org/10.1016/j.geomorph.2010.04.009>
- Cruden DM, Varnes DJ (1996) Landslide types and processes. In: Turner AK, Schuster RL (eds) *Landslides: investigation and mitigation*. National Academy Press, Washington, D. C., pp 36–75
- Daehne A, Corsini A (2012) Kinematics of active earthflows revealed by digital image correlation and DEM subtraction techniques applied to multi-temporal LiDAR data. *Earth Surf Process Landf* 38(6):640–654. <https://doi.org/10.1002/esp.3351>
- Del Soldato M, Riquelme A, Bianchini S, Tomàs R, Di Martire D, De Vita P, Moretti S, Calcaterra D (2018) Multisource data integration to investigate one century of evolution for the Agnone landslide (Molise, southern Italy). *Landslides* 15(11):2113–2128. <https://doi.org/10.1007/s10346-018-1015-z>
- Delacourt C, Allemand P, Casson B, Vadon H (2004) Velocity field of the “la clapière” landslide measured by the correlation of aerial and quickbird satellite images. *Geophys Res Lett* 31. <https://doi.org/10.1029/2004gl020193>
- Delacourt C, Allemand P, Berthier E, Raucoules D, Casson B, Grandjean P, Pambrun C, Varel E (2007) Remote-sensing techniques for analysing landslide kinematics: A review. *Bull Soc Geol Fr* 178:89–100. <https://doi.org/10.2113/gssgfbull.178.2.89>
- Delbridge BG, Bürgmann R, Fielding E, Hensley S, Schulz WH (2016) 3d surface deformation derived from airborne interferometric uavsar: application to the slumgullion landslide. *J Geophys Res Solid Earth*. <https://doi.org/10.1002/2015jb012559>
- DeLong SB, Prentice CS, Hilley GE, Ebert Y (2012) Multitemporal alsm change detection, sediment delivery, and process mapping at an active earthflow. *Earth Surf Process Landf* 37:262–272. <https://doi.org/10.1002/esp.2234>
- DeLong SB, Hilley GE, Prentice CS, Crosby CJ, Yokelson IN (2017) Geomorphology, denudation rates, and stream channel profiles reveal patterns of mountain building adjacent to the San Andreas fault in northern California, USA. *Geol Soc Am Bull* 129:732–749. <https://doi.org/10.1130/b31551.1>
- Guerrero L, Bertello L, Cardozo N, Berti M, Grelle G, Revellino P (2017) Unsteady sediment discharge in earth flows: a case study from the Mount Pizzuto earth flow,

- southern Italy. *Geomorphology* 295:260–284. <https://doi.org/10.1016/j.geomorph.2017.07.011>
- Handwerger AL, Roering JJ, Schmidt DA (2013) Controls on the seasonal deformation of slow-moving landslides. *Earth Planet Sci Lett* 377:239–247. <https://doi.org/10.1016/j.epsl.2013.06.047>
- Handwerger AL, Roering JJ, Schmidt DA, Rempel AW (2015) Kinematics of earthflows in the northern California coast ranges using satellite interferometry. *Geomorphology* 246:321–333. <https://doi.org/10.1016/j.geomorph.2015.06.003>
- Handwerger AL, Huang M-H, Fielding EJ, Booth AM, Burgmann R (2019) A shift from drought to extreme rainfall drives a stable landslide to catastrophic failure. *Sci Rep* 9:1–12. <https://doi.org/10.1038/s41598-018-38300-0>
- Hanks TC (2000) The age of scarplike landforms from diffusion-equation analysis. *Quat Geochronol Methods Applic* 4:313–338. <https://doi.org/10.1029/Rf004p0313>
- Heid T, Käbb A (2012) Evaluation of existing image matching methods for deriving glacier surface displacements globally from optical satellite imagery. *Remote Sens Environ* 118:339–355. <https://doi.org/10.1016/j.rse.2011.11.024>
- Hillel GE, Burgmann R, Ferretti A, Novali F, Rocca F (2004) Dynamics of slow-moving landslides from permanent scatterer analysis. *Science* 304:1952–1955. <https://doi.org/10.1126/science.1098821>
- Hutchinson JN (1983) Methods of locating slip surfaces in landslides. *Bull Assoc Eng Geol* 20:235–252
- Iverson RM (2005) Regulation of landslide motion by dilatancy and pore pressure feedback. *J Geophys Res* 110. <https://doi.org/10.1029/2004jf000268>
- Iverson RM, Major JJ (1987) Rainfall, ground-water flow, and seasonal movement at Minor Creek landslide, northwestern California: physical interpretation of empirical relations. *Geol Soc Am Bull* 99:579–594
- Jaboyedoff M, Oppikofer T, Abellán A, Derron M-H, Loye A, Metzger R, Pedrazzini A (2010) Use of lidar in landslide investigations: a review. *Nat Hazards* 61:5–28. <https://doi.org/10.1007/s11069-010-9634-2>
- Käbb A (2002) Monitoring high-mountain terrain deformation from repeated air-and spaceborne optical data: examples using digital aerial imagery and ASTER data. *ISPRS J Photogramm Remote Sens* 57(1–2):39–52. [https://doi.org/10.1016/S0924-2716\(02\)00114-4](https://doi.org/10.1016/S0924-2716(02)00114-4)
- Keefer DK and Johnson AM (1983) Earth flows: Morphology, mobilization, and movement. *Geological Survey Professional Paper* 1264
- Kelsey HM (1978) Earthflows in Franciscan melange, Van Duzen River basin, California. *Geology* 6:361–364. [https://doi.org/10.1130/0091-7613\(1978\)6<361:Eifmvd>2.0.Co;2](https://doi.org/10.1130/0091-7613(1978)6<361:Eifmvd>2.0.Co;2)
- Kelsey HM (1980) A sediment budget and an analysis of geomorphic process in the Van Duzen River basin, north coastal California, 1941–1975 - summary. *Geol Soc Am Bull* 91:190–195. [https://doi.org/10.1130/0016-7606\(1980\)91<190:Asbaaa>2.0.Co;2](https://doi.org/10.1130/0016-7606(1980)91<190:Asbaaa>2.0.Co;2)
- Kuglin CD, Hines DC (1975) The phase correlation image alignment method. In *Proceedings of the IEEE 1975 International Conference on Cybernetics and Society*, New York, NY, pp 163–165
- Lacroix P, Berthier E, Maquerhua ET (2015) Earthquake-driven acceleration of slow-moving landslides in the Colca valley, Peru, detected from Pléiades images. *Remote Sens Environ* 165:148–158. <https://doi.org/10.1016/j.rse.2015.05.010>
- Larsen IJ, Montgomery DR (2012) Landslide erosion coupled to tectonics and river incision. *Nat Geosci* 5:468–473. <https://doi.org/10.1038/ngeo1479>
- Lawson AC (1908) The California earthquake of April 18, 1906: Report of the state earthquake investigation commission. *Carnegie Institution of Washington*, Washington, D. C.
- Leprince S, Barbot S, Ayoub F, Avouac JP (2007) Automatic and precise orthorectification, coregistration, and subpixel correlation of satellite images, application to ground deformation measurements. *IEEE Trans Geosci Remote Sens* 45:1529–1558. <https://doi.org/10.1109/Tgrs.2006.888937>
- Lucier A, de Jong SM, Turner D (2013) Mapping landslide displacements using structure from motion (SfM) and image correlation of multi-temporal UAV photography. *Prog Phys Geogr* 38(1):97–116. <https://doi.org/10.1177/0309133313515293>
- Mackey BH, Roering JJ (2011) Sediment yield, spatial characteristics, and the long-term evolution of active earthflows determined from airborne lidar and historical aerial photographs, Eel River, California. *Geol Soc Am Bull* 123:1560–1576. <https://doi.org/10.1130/B30306.1>
- Mackey BH, Roering JJ, McKean JA (2009) Long-term kinematics and sediment flux of an active earthflow, Eel River, California. *Geology* 37:803–806. <https://doi.org/10.1130/g30136a.1>
- Malet JP, Maquaire O, Calais E (2002) The use of global positioning system techniques for the continuous monitoring of landslides: application to the super-Sauze earthflow (Alpes-de-Haute-Provence, France). *Geomorphology* 43:33–54. [https://doi.org/10.1016/S0169-555x\(01\)00098-8](https://doi.org/10.1016/S0169-555x(01)00098-8)
- Manson MW, Huyette CJ, Wills CJ, Huffman ME, Smelser MG, Fuller ME, Domrose C, Gutierrez C, (2006) Landslides in the Highway 1 corridor between Bodega Bay and Fort Ross, Sonoma county, California. *California Department of Conservation, California Geological Survey, Special Report*, p 196
- Massey CI, Petley DN, McSaveney MJ (2013) Patterns of movement in reactivated landslides. *Eng Geol* 159:1–19. <https://doi.org/10.1016/j.enggeo.2013.03.011>
- Massey CI, Petley DN, McSaveney MJ, Archibald G (2016) Basal sliding and plastic deformation of a slow, reactivated landslide in New Zealand. *Eng Geol* 208:11–28. <https://doi.org/10.1016/j.enggeo.2016.04.016>
- McSaveney MJ, Griffiths GA (1987) Drought, rain, and movement of a recurrent earthflow complex in New Zealand. *Geology* 15:643–646. [https://doi.org/10.1130/0091-613\(1987\)15<643:Dramoa>2.0.Co;2](https://doi.org/10.1130/0091-613(1987)15<643:Dramoa>2.0.Co;2)
- Messerli A, Grinsted A (2015) Image georectification and feature tracking toolbox: Imgraft. *Geosci Instrum Methods Data Syst* 4:23–34. <https://doi.org/10.5194/gi-4-23-2015>
- Mikkelsen PE (1996) Field instrumentation. In: Turner AK, Schuster RL (eds) *Landslides: investigation and mitigation*. National Academy Press, Washington, D. C, pp 278–316
- Miller DJ, Sias J (1998) Deciphering large landslides: linking hydrological, groundwater and slope stability models through GIS. *Hydrol Process* 12:923–941. [https://doi.org/10.1002/\(Sici\)1099-1085\(199805\)12:6<923::Aid-Hyp663>3.0.Co;2-3](https://doi.org/10.1002/(Sici)1099-1085(199805)12:6<923::Aid-Hyp663>3.0.Co;2-3)
- Muhs DR, Rockwell TK, Kennedy GL (1992) Late quaternary uplift rates of marine terraces on the Pacific coast of North America, southern Oregon to Baja California Sur. *Quat Int* 15(16):121–133
- Muhs DR, Kennedy GL, Rockwell TK (1994) Uranium-series ages of marine terrace corals from the Pacific coast of North America and implications for last-interglacial sea level history. *Quat Res* 42:72–87
- Muhs DR, Prentice C, Merritts DJ (2003) Marine terraces, sea level history and Quaternary tectonics of the San Andreas Fault on the coast of California. In: Easterbrook DJ (ed) *Quaternary geology of the United States*. Desert Research Institute, Reno, Nevada, pp 1–18
- Oppenheim AV, Schafer RW (2010) *Discrete-time signal processing*. Pearson, Upper Saddle River, New Jersey
- Oppikofer T, Jaboyedoff M, Blikra L, Derron M-H, Metzger R (2009) Characterization and monitoring of the Åknes rockslide using terrestrial laser scanning. *Nat Hazards Earth Syst Sci* 9:1003–1019
- Ouimet WB, Whipple KX, Royden LH, Sun Z, Chen Z (2007) The influence of large landslides on river incision in a transient landscape: eastern margin of the Tibetan plateau (Sichuan, China). *Geol Soc Am Bull* 119:1462–1476. <https://doi.org/10.1130/b26136.1>
- Prior DB, Stephens N (1972) Some movement patterns of temperate mudflows: examples from northeastern Ireland. *Geol Soc Am Bull* 83:2533–2544. [https://doi.org/10.1130/0016-7606\(1972\)83\[2533:Smpotmj\]2.0.Co;2](https://doi.org/10.1130/0016-7606(1972)83[2533:Smpotmj]2.0.Co;2)
- Raucoules D, De Michele M, Malet JP, Ulrich P (2013) Time-variable 3D ground displacements from high-resolution synthetic aperture radar (SAR). Application to La Valette landslide (South French Alps). *Remote Sens Environ* 139:198–204. <https://doi.org/10.1016/j.rse.2013.08.006>
- Reid ME (1994) A pore-pressure diffusion model for estimating landslide-inducing rainfall. *J Geol* 102(6):709–717. <https://doi.org/10.1086/629714>
- Riquelme A, Del Soldato M, Tomás R, Cano M, Bordehore LJ, Moretti S (2019) Digital landform reconstruction using old and recent open access digital aerial photos. *Geomorphology* 329:206–223. <https://doi.org/10.1016/j.geomorph.2019.01.003>
- Roering JJ, Mackey BH, Handwerger AL, Booth AM, Schmidt DA, Bennett GL, Cerovski-Darriau C (2015) Beyond the angle of repose: a review and synthesis of landslide processes in response to rapid uplift, Eel River, Northern California. *Geomorphology* 236:109–131. <https://doi.org/10.1016/j.geomorph.2015.02.013>
- Safran EB, Anderson SW, Mills-Novoa M, House PK, Ely L (2011) Controls on large landslide distribution and implications for the geomorphic evolution of the southern interior Columbia River basin. *Geol Soc Am Bull* 123:1851–1862. <https://doi.org/10.1130/b30061.1>
- Sambridge M, Braun J, McQueen H (1995) Geophysical parametrization and interpolation of irregular data using natural neighbours. *Geophys J Int* 122:837–857. <https://doi.org/10.1111/j.1365-246X.1995.tb06841.x>
- Scheingross JS, Minchew BM, Mackey BH, Simons M, Lamb MP, Hensley S (2013) Fault-zone controls on the spatial distribution of slow-moving landslides. *Geol Soc Am Bull* 125:473–489. <https://doi.org/10.1130/b30719.1>
- Schmidt KM, Montgomery DR (1995) Limits to relief. *Science* 270:617–620. <https://doi.org/10.1126/science.270.5236.617>
- Schulz WH, Smith JB, Wang GH, Jiang Y, Roering JJ (2018) Clayey landslide initiation and acceleration strongly modulated by soil swelling. *Geophys Res Lett* 45:1888–1896. <https://doi.org/10.1002/2017gl076807>

- Sibson R (1981) A brief description of natural neighbour interpolation. In: Barnett V (ed) *Interpreting multivariate data*. Wiley, New York, pp 21–36
- Simoni A, Ponza A, Picotti V, Berti M, Dinelli E (2013) Earthflow sediment production and Holocene sediment record in a large Apennine catchment. *Geomorphology* 188:42–53. <https://doi.org/10.1016/j.geomorph.2012.12.006>
- Solari L, Raspini F, Del Soldato M, Bianchini S, Ciampalini A, Ferrigno F, Tucci S, Casagli N (2018) Satellite radar data for back-analyzing a landslide event: the Ponzano (Central Italy) case study. *Landslides* 15(4):773–782. <https://doi.org/10.1007/s10346-018-0952-x>
- Swanson FJ, Swanston DN (1977) Complex mass-movement terrains in the western Cascade Range. *Oregon Rev Eng Geol* 11:113–124
- Tarolli P, Dalla Fontana G (2009) Hillslope-to-valley transition morphology: new opportunities from high resolution DTMs. *Geomorphology* 113:47–56. <https://doi.org/10.1016/j.geomorph.2009.02.006>
- Teza G, Galgaro A, Zaltron N, Genevois R (2007) Terrestrial laser scanner to detect landslide displacement fields: a new approach. *Int J Remote Sens* 28(16):3425–3446. <https://doi.org/10.1080/01431160601024234>
- Tofani V, Segoni S, Agostini A, Catani F, Casagli N (2013) Use of remote sensing for landslide studies in Europe. *Nat Hazards Earth Syst Sci* 13(2):299–309. <https://doi.org/10.5194/nhess-13-299-2013>
- Tong X, Schmidt D (2016) Active movement of the Cascade landslide complex in Washington from a coherence-based InSAR time series method. *Remote Sens Environ* 186:405–415. <https://doi.org/10.1016/j.rse.2016.09.008>
- U.S. Army Corps of Engineers (1990) *Engineering and design, settlement analysis: engineer manual 1110–1-1904*. U.S. Army Corps of Engineers, Washington
- Van Puymbroeck N, Michel R, Binet R, Avouac J-P, Taboury J (2000) Measuring earthquakes from optical satellite images. *Appl Opt* 39(20):3486–3494. <https://doi.org/10.1364/AO.39.003486>
- Ventura G, Vilaro G, Terranova C, Sessa EB (2011) Tracking and evolution of complex active landslides by multi-temporal airborne LiDAR data: the Montaguto landslide (Southern Italy). *Remote Sens Environ* 115(12):3237–3248. <https://doi.org/10.1016/j.rse.2011.07.007>
- Wartman J, Montgomery DR, Anderson SA, Keaton JR, Benoît J, dela Chapelle J, Gilbert R (2016) The 22 March 2014 Oso landslide, Washington, USA. *Geomorphology* 253:275–288. <https://doi.org/10.1016/j.geomorph.2015.10.022>
- Zerathe S, Lacroix P, Jongmans D, Marino J, Taïpe E, Wathélet M, Pari W, Smoll LF, Norabuena E, Guillier B, Tataro L (2016) Morphology, structure and kinematics of a rainfall controlled slow-moving Andean landslide, Peru. *Earth Surf Process Landf* 41(11):1477–1493. <https://doi.org/10.1002/esp.3913>

Electronic supplementary material The online version of this article (<https://doi.org/10.1007/s10346-020-01364-z>) contains supplementary material, which is available to authorized users.

A. M. Booth (✉) · **J. C. McCarley** · **J. Nelson**

Department of Geology,
Portland State University,
17 Cramer Hall, 1721 SW Broadway, Portland, OR 97201, USA
Email: boothad@pdx.edu